If CW approaches CWmax, CW is set to CWmax until the maximal retransmission number, and frames are discarded.

A receiving node sends an ACK frame after SIFS (Short Inter Frame Space) time to inform the sending node the correct reception of data frames. If the sending node does not receive the ACK frame, it assumes that the transmission is lost and it retransmits data frames again. The IFS time is a minimal time interval for sending information.

2) Pure ALOHA

In the pure ALOHA protocol, nodes transmit whenever they have data to send. Then nodes listen to positive ACK (AC-Knowledgement) on a separate link. If timeout (collision), the node waits a random time and then retransmits. The number of request to send packets follows the Poisson distribution. The probability of the collision of packets is given by

$$P = 1 - e^{-2\lambda\tau}, \tag{6}$$

where λ is the arrival rate of packets, τ is the transmission time of one packet. We assumed that λ is given by

$$\lambda = \frac{2\tau}{(CWmin \times slottime)/2}. \tag{7}$$

B. Proposed protocol

We propose a new protocol where the backoff time is randomly generated in the interval $[0, CW]$, where $CWmin$ is the number of RFD nodes. Essentially, the value of CWmin is constant and equal to the number of RFD nodes. We assume that leader can number FD nodes by receiving the signal from each RFD node.

Additionally, RFD nodes are grouped into two groups in this protocol. So that half of the RFD nodes monitors while the other half transmits, alternatively. Consequently, CWmin would be half the number of RDF nodes in the cluster

$$CWmin = \frac{M}{2}, \tag{8}$$

where M is the number of RFD nodes in the cluster.

We aim to control the temperature increment in a certain period of time compared with existing protocols.

V. COMPUTER SIMULATION

A. Simulation setup

Each RFD node has two modes. In one mode the RFD node takes health data (monitoring mode), while in the other mode the RFD transmits to the leader (transmission mode). In this simulation, we calculate the temperature increment only in the leader position. Consequently, when each RFD nodes is in monitoring mode, the temperature in the a position of the leader does not increase, and in fact it decreases due to the cooling effect of surrounding blood flow.

Additionally, the time of transmission to the medical server outside the body from the leader is fairly shorter as compared with its time of reception from each RFD nodes. So, we assume that almost of the thermal influence of the leader in active

mode is generated while RFD transmission mode. Therefore, the time that the leader is affected thermal influence is approximated the time of RFD transmission mode.

Assuming that the monitoring mode plus transmitting mode is one cycle, after ten cycles the leadership is switched to another FFD in order to decrease the thermal influence.

Parameters in this simulation are shown in Table 2. We compare the collision rate, the transmitting efficiency and the highest temperature increment during certain a long period of time for each protocol.

Table 2: Parameters and their values of mucsle and blood.

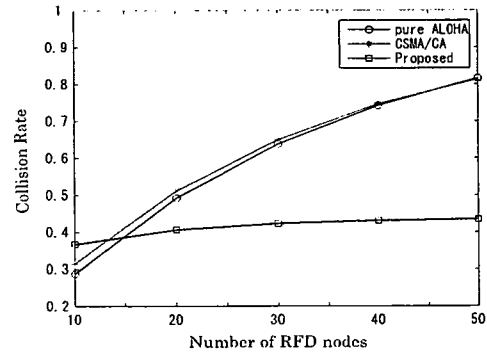| parameter	value	parameter	value
Bit rate	250kbps	Payload	500bit,
slot time	144μs	Packet	50
SIFS time	192μs	CW_{min}	15
DIFS time	400μs	CW_{max}	1023
ACK time	352μs		

B. Simulation result

Figure 5: Collision rate characteristic

In Fig. 5, the collision rate depends on the number of RFD nodes in pure ALOHA, CSMA/CA and proposed protocol, respectively. The collision rate is defined as the rate of the number of packets collision over the number of transmission request.

In addition, we change the number of RDF nodes in the cluster from 10 to 50 at intervals of 10. As shown in Fig. 5, there is not difference between pure ALOHA and CSMA/CA. Moreover, the change of the collision rate increases with the number RFD nodes. On the other hand, we can control the collision rate considerably with the proposed protocol, even if the number of RFD nodes increases.

We consider that the reason of this result is the decrease of the rate of overlap of minimum backoff time. This decrease is occured by expansion of CW which is depend on the number of RFD nodes.

Figure 6 illustrates the transmitting efficiency depending on the number of RFD nodes in each protocol.
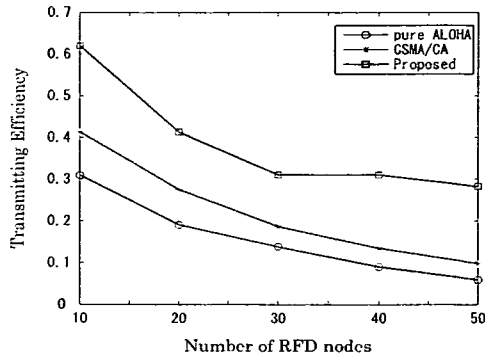
Figure 6: Transmitting efficiency characteristic

The transmission efficiency is defined as the rate of the data transmission time over the entire communication time.

As shown in Figure 6, CSMA/CA shows around 10% better performance than pure ALOHA. Moreover, the proposed protocol improves the performance around 20% compared to CSMA/CA.

We consider that the factor of this result is the decrease of the number of collision. We comprehend that the decrease make transmitting efficiency be better.
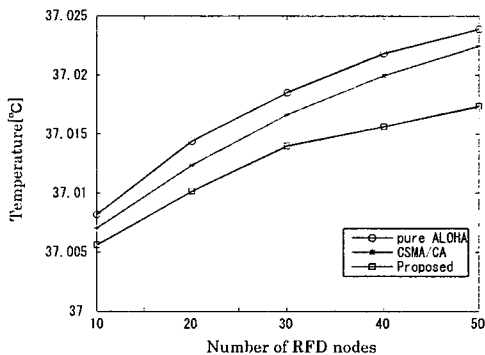
Figure 7: highest temperature characteristic

Finally, Figure 7 shows the highest temperature during 2000 seconds, where leaders can switch several times depending on the number of nodes in each protocols. Why we apply the highest temperature during 2000 seconds is that the temperature of leader in each situation is saturated after a time. So, we assume that the highest temperature during 2000 seconds is approximated saturated temperature.

As shown in Figure 7, this performance is similar to Figure 6. If the transmitting efficiency is low, the period of RFD transmission mode would be expected to be shorten. And then, the time the leader is affected thermal influence by exposing radiation would shorten. So we can conclude that the less performance the larger the thermal influence. Therefore the proposed protocol can control the thermal influence better than the existing protocols pure ALOHA and CSMA/CA.

VI. CONCLUSIONS

In this paper, we propose a novel MAC protocol, which controls the thermal influence in an implanted body area network and confirms its performance. With future advances in technology, we can expect the proposal can be used in specific applications for implanted body area networks.

In a future work, we plan to consider change of radiation for each mode, and a different complex medium at a given specific position of implanted nodes. Then, we can study the proposed MAC protocol based on the conditions mentioned before.

REFERENCES

[1] W. R. Heinzelman, A. Chandrakasan, and H. Balakrishnan."Energy-Efficient Communication Protocols for Wireless Microsensor Networks"In Hawaii International Conference on System Sciences,2000

[2] Shankar, V. Natarajan, A. Gupta, S.K.S. Schwiebert, L. Dept. of Comput. Sci. Eng., Arizona State Univ., Tempe, AZ, USA"Energy-efficient protocols for wireless communication in biosensor networks" Personal, Indoor and Mobile Radio Communications, 2001 12th IEEE International Symposium on 30 Sept.-3 Oct. 2001 Volume: 1

[3] Naoki KUSE, Koji ISHIBASHI, Satoshi MATSUDA, Hiroki HARADA, and Ryuji KOHNO, "A study on In Vivo Wireless Communication Based on Body Temperature Elevation",IEICE Technical Report RCS2005-228(2006-3).

[4] [Online] Available: http://www.remcom.com

[5] Qinghui Tang, Naveen Tummala, Sandeep K. S. Gupta, Senior Member, IEEE, and Loren Schwiebert Senior Member, IEEE,"Communication Scheduling to Minimize Thermal Effects of Implanted Biosensor Networks in Homogeneous Tissue" Biomedical Engineering, IEEE Transactions on July 2005 Volume: 52, Issue: 7 pp 1285- 1294

[6] Qinghui Tang, Naveen Tummala, Sandeep K. S. Guptal, and Loren Schwiebert2"TARA: Thermal-Aware Routing Algorithm for Implanted Sensor Networks"Computer Design: VLSI in Computers and Processors, 2004. ICCD 2004. Proceedings. IEEE International Conference on 11-13 Oct. 2004 pp 430- 437

[7] Jose A.Gutierrez, Edgar H.Callaway,Jr., Raymond L.Barrett,Jr.,"Low-Rate Wireless Personal Area Networks"Published by Standards Information Network IEEE Press.

POSITION ESTIMATION METHOD OF MEDICAL IMPLANTED DEVICES USING ESTIMATION OF PROPAGATION VELOCITY INSIDE THE HUMAN BODY

Makoto Kawasaki, Hiroki Harada, Ryuji Kohno

Division of Physics, Electrical and Computer Engineering, Yokohama National University

79-5 Tokiwadai, Hodogaya, Yokohama, 240-8501, Japan

Tel: +81-45-339-4116, Fax: +81-45-338-1176

E-mail: makoto,hhiroki@kohnolab.dnj.ynu.ac.jp,kohno@ynu.ac.jp

ABSTRACT

Recently, wireless communication devices in the field of medical implant, such as cardiac pacemakers and capsule endoscopes, have been studied and developed to improve healthcare systems. Especially it is very important to know the range and position of each device because it will contribute to an optimization of the transmission power. We adopt the time-based approach of position estimation using ultra wideband (UWB) signals. However, the propagation velocity inside the human body differs in each tissue. In this paper, we propose a position estimation method using an estimation of the propagation velocity inside the human body. In addition, we show by computer simulation that the proposal method can perform accurate positioning with a size of medical implanted devices such as a medicine capsule.

I. INTRODUCTION

Recently, wireless communication devices in the field of medical implant (cardiac pacemaker and capsule endoscope and so on) are studied extensively towards practical use. In the future, by transmitting vital data from one device to another implanted device in a network of medical implants, we can observe the body's condition and to detect any possible problem in the human body at anytime and anywhere. These can be a great help for doctors to diagnose and to cure diseases.[1]

Considering that transmitted information of vital data is highly important and the need for long-lasting batteries, it is important that wireless communications of medical implanted devices to be highly-reliable with low transmission power consumption. In that regard, it is very important to know ranging and position of each device, because that can help to the optimization of the transmission power. In this paper, we employ UWB systems as the transmission signals, because those achieve high resolution and low transmission power. Thus, we propose a method of position estimation of medical implanted devices inside the human body.

In free space, a type of position estimation algorithm is time-based technique. Such a technique relies on measurements of travel time of signals between nodes. So, range and position can be known because the propagation velocity of microwaves in free space is constant. On the other hand, the human body is formed of various organs with complex structures. Furthermore, each organ has different characteristics of conductivity and relative permittivity. So, propagation velocity inside human body is expressed as a function of the relative permittivity. For this reason, medical implanted devices placed in different positions cause different propagation velocities due to the EM waves travel through different tissues or organs. As a result, position estimation errors may occur.

In this paper, we study the position estimation of medical implanted devices based on the propagation characteristic inside the human body. We use the finite-difference time-domain (FDTD) method, which has been widely used to simulate the propagation of electromagnetic waves in biomedical tissues, considering the complex structure of the human body. On the premise that images of inside human body can be obtained by magnetic resonance imaging (MRI) and computer tomography (CT), we divide the images into regions in order to estimate the relative permittivity of such regions. Then, we estimate the propagation velocity between implanted devices. Finally, we estimate the position of medical implanted devices with a time-based positioning approach.

This paper is organized as follows: In Section 2, position estimation using UWB signal is described. In Section 3, some basic characteristics of EM wave propagation and properties of dielectric materials which involve the human body tissue are described. The proposed position estimation method is presented in Section 4. Simulation results are drawn in Section 5. Finally, conclusions are delineated in Section 6.

II. POSITIONING USING ULTRA WIDEBAND SIGNALS

Locating a node in a wireless system involves the collection of location data from radio signals traveling between the target node and a number of reference nodes. Depending on the positioning technique, the angle of arrival (AOA), the signal strength(SS), or time delay information can be used to determine the location of a node. The AOA technique measures the angles between a given node and a number of reference nodes to estimate the location, while the SS and time-based approaches estimate the distance between nodes by measuring the energy and the travel time of the received signal, respectively.

Particularly, the accuracy of a time-based approach can be improved by increasing the SNR or the effective signal's bandwidth. Since UWB signals have very large bandwidth, it allows extremely accurate position estimation through time-based techniques. The main time-based techniques are the time of arrival (TOA) technique and the time difference of arrival (TDOA) technique. In the former technique, there is synchronization between a given node and the reference nodes. Whereas in the latter technique, there is synchronization among the reference nodes. An estimate of the arrival's time is obtained using a correlation receiver. In this approach the time

shift of the template signal that yields the largest cross correlation with the received signal gives the desired estimate. Moreover, the TOA-based scheme estimates the location of the node using the least squares (LS) approach. The LS approach is given by

$$\hat{\theta} = min \sum_{i=1}^{N} [\tau_i - d_i(\theta)/c]^2, \qquad (1)$$

where N is the number of reference nodes, τ_i is the ith TOA measurement, $d_i(\theta) = \|\theta - \theta_i\|$ is the distance between the given node and the ith reference node, with θ and θ_i denoting their locations, respectively.[2]

In this paper, we adopt the time-based LS approach.

III. RADIO PROPAGATION IN A MEDIUM

A. Electric constant of human body tissues

A human body consists of various organs with complex structures. Furthermore, each organ has different characteristics of conductivity and permittivity.

We should consider the frequency band when we try to estimate the position of implanted devices using UWB radios. Indeed, the electromagnetic wave propagation in dispersive biological tissues is frequency dependent on permittivity and conductivity. The Cole-Cole model describes the frequency dependency of the complex permittivity as

$$\varepsilon_r(\omega) = \varepsilon_\infty + \sum_{n=1}^{M} \frac{\Delta\varepsilon_n}{1 + (j\omega\tau_n)^{1-\alpha_n}} + \frac{\sigma}{j\omega\varepsilon_0}, \qquad (2)$$

where M is the order of the Cole-Cole model, ε_∞ is the high frequency permittivity, τ_I is the relaxation time, $\Delta\varepsilon_I$ is the pole amplitude, α_I is a measure of the broadening of dispersion, and σ is the conductivity. These parameter are different for different body tissues. Then, the relative permittivity $\varepsilon_r(\omega)$ is the real part of complex permittivity, and the imaginary part is the conductivity.[1] Figure 1 shows the relative permittivity and conductivity of muscle and fat.
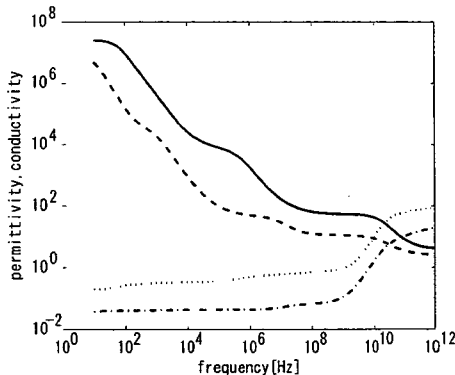

Figure 1: Dielectric parameters of muscle and fat

Furthermore, the propagation velocity of a homogeneous tissue is given by

$$v(\omega) = \frac{c}{\sqrt{\varepsilon_r(\omega)}}, \qquad (3)$$

where c is the velocity of light in the free space and $\varepsilon_r(\omega)$ is the relative permittivity of a human tissue. So propagation velocity has frequency dependency and differs by different body tissues.

B. Propagation of Electromagnetic Waves in Dielectric Material

Propagation of EM waves in dielectric materials such as in a human body, is different from propagation in the free space, because of non-zero conductivity and higher permittivity of human body tissues. In a lossy medium, the permittivity is replaced by the complex permittivity. Now, we consider a plane wave that is traveling in the positive z direction.

$$E = E_0 e^{-jkz}, \qquad (4)$$

where k is the wave number and z is propagated distance. Wave number k is also complex, therefore electric field and magnetic field is attenuated by traveling. Wave number is generally separated into realistic component and imaginary component.

$$k = \beta - j\alpha, \qquad (5)$$

$$\alpha = \omega\sqrt{\mu\varepsilon}\sqrt{\frac{1}{2}\left(\sqrt{1 + (\frac{\sigma}{\omega\varepsilon})^2} - 1\right)}, \qquad (6)$$

$$\beta = \omega\sqrt{\mu\varepsilon}\sqrt{\frac{1}{2}\left(\sqrt{1 + (\frac{\sigma}{\omega\varepsilon})^2} + 1\right)}, \qquad (7)$$

where α is the attenuation constant and β is the phase constant.[1]

IV. PROPOSED METHOD OF POSITION ESTIMATION

A. Relative permittivity of homogeneous tissue

Although relative permittivity of a human body tissue is frequency dependent, the arrival's time is obtained by using a correlation receiver. So, the relative permittivity can be rewritten as

$$\varepsilon_r = \left(\frac{c\, t_a}{d}\right)^2, \qquad (8)$$

where t_a is the arrival's time, and d is the propagation distance in a homogeneous tissue.

We analyze the relative permittivity of human homogeneous tissues using the FDTD method.[3] Figure 2 shows the relative permittivity in function of the distance d. We take the average relative permittivity of eight tissues, which are listed in Table 1.
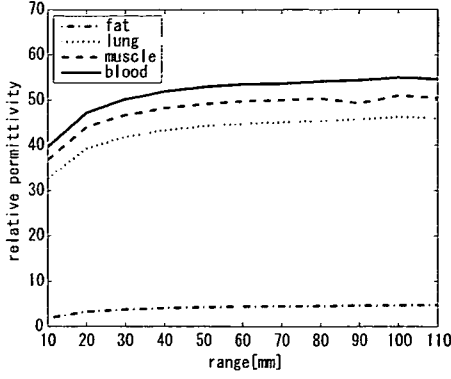
Figure 2: Distance property of relative permittivity of human homogeneous tissues

Tissue	muscle	fat	blood	intestine
ε_r	47.83	4.08	51.59	50.67
Tissue	stomach	tendon	bone	bladder
ε_r	56.99	37.61	17.09	64.63

Table 1: The average relative permittivity of human body tissues

B. Proposed method of Position Estimation

We proposed a position estimation method by estimating the propagation velocity inside of a human body. In addition to it, we calculate the propagation time from arbitrary tag points to node points (whose position is known) by using the estimated propagation velocity. Finally, we estimate the position of medical implanted devices using the LS approach.

The images of inside of the human body are acquired beforehand from a MRI or CT system. Our proposed method uses four medical implanted devices, whose locations are known, and we call them "node" in this paper. On the other hand, there is a medical implanted device, whose location is unknown, and we call it "tag" in this paper.

Our proposed method is composed of two stages. It is very difficult to estimate the real propagation velocity from all arbitrary tag points to node point directly. So, the real propagation velocity is estimated by the images of inside human body obtained from MRI or CT systems beforehand. So, we have large volumes of data of the real propagation velocity. Hence, we estimate the propagation velocity with two stages to simplify the estimation and to reduce the amount of data.

1) First stage

The procedure of the first stage is as follows. At first, we calculate the average relative permittivity of the region delimited by four nodes. The average relative permittivity ε_{ave} and propagation velocity v_{ave} are calculated as

$$\varepsilon_{ave} = \sum_{i=1}^{I} (\varepsilon_{t(i)} \, p_{t(i)}), \qquad (9)$$

$$v_{ave} = \frac{c}{\sqrt{\varepsilon_{ave}}}, \qquad (10)$$

where n is node number, I total number of tissues, $\varepsilon_{t(i)}$ is the ε_r of a homogeneous tissue listed in Table 1, and $p_{t(i)}$ is a percentage of the ith tissue.[4]
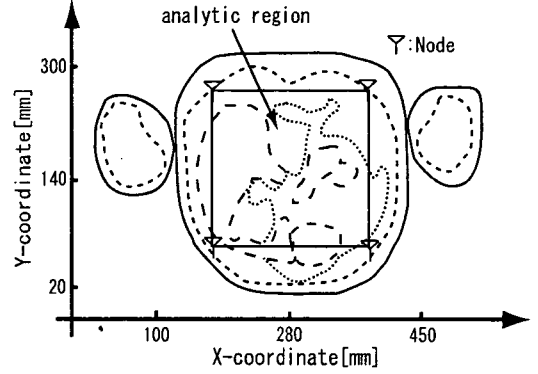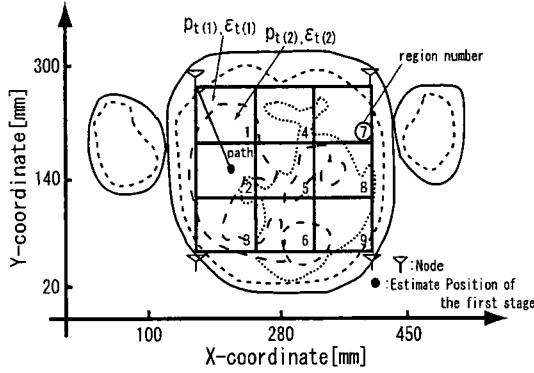

Figure 3: System model of the first stage

Secondly, we calculate the propagation time $t^1_{n(x,y)}$ from four nodes to an arbitrary point in the studied region using v_{ave}. The propagation time in the first stage for the nth node $t^1_{n(x,y)}$ is calculated as

$$t^1_{n(x,y)} = \frac{d_{n(x,y)}}{v_{ave}}, \qquad (11)$$

where x is x-coordinate of an arbitrary point, y is y-coordinate of an arbitrary point, $d_{n(x,y)}$ is a length of a path from an arbitrary point to the four nodes, respectively. Also, x, y have 1 mm of separation.

Then, we estimate the travel times t_n of the received signal from the tag point to the four nodes by using a correlation receiver. In this approach, the desired estimation is given by the time shift of the template signal that yields the largest cross correlation with the received signal.

Finally, we estimate the position of tag using the LS approach.

$$\theta(x, y)_1 = min \sum_{n=1}^{4} [t_n - t^1_{n(x,y)}]^2, \qquad (12)$$

where $\theta(x, y)_1$ is the estimate position of the first stage.

2) Second stage

In the stage, we use $\theta(x, y)_1$, which is obtained from Equation 12.

Firstly, we divide the images inside of the human body into several regions and estimate relative permittivity of a respective region. A relative permittivity of one region is calculated as

$$\varepsilon_j = \sum_{i=1}^{I} (\varepsilon_{t(i)} \, p_{t(i)}), \qquad (13)$$

where j is a region number, i is a tissue number, ε_j is an average relative permittivity of jth region, $\varepsilon_{t(i)}$ is the ε_r of a homogeneous tissue listed in Table 1, and $p_{t(i)}$ is a percentage of the ith tissue in the jth region.

Secondly, we estimate the relative permittivity ε_n and propagation velocity v_n of the paths from four nodes to $\theta(x,y)_1$.

$$\varepsilon_n = \frac{\sum_{k=1}^{K}(\varepsilon_k\, d_k)}{d_{all}}, \tag{14}$$

$$v_n = \frac{c}{\sqrt{\varepsilon_n}}, \tag{15}$$

where K is a number of regions through the propagation path from the nth node to $\theta(x,y)_1$, d_k is a length of the path through the kth region, and d_{all} is a length of the path from n^{th} node to $\theta(x,y)_1$.

Figure 4: (3×3) regions system model of the second stage

Then, we calculate the propagation time $t^2_{n(x,y)}$ from four nodes to an arbitrary point using v_n. The propagation time $t^2_{n(x,y)}$ is calculated as

$$t^2_{n(x,y)} = \frac{d_{n(x,y)}}{v_n}, \tag{16}$$

where x is x-coordinate of an arbitrary point, y is y-coordinate of an arbitrary point, and $d_{n(x,y)}$ is a length of a path from an arbitrary point to four nodes, respectively. And x, y have 1 mm of separation.

Finally, we estimate the position of tag using the LS approach.

$$\theta(x,y)_2 = min\sum_{n=1}^{4}[t_n - t^2_{n(x,y)}]^2, \tag{17}$$

where t_n is the travel time of the received signal from tag to the four nodes, and $\theta(x,y)_2$ is the estimate position of the second stage.

V. SIMULATION RESULTS

This section presents simulations to demonstrate the performance of the proposed method.

A. Simulation model

Figure 5 shows the simulation image obtained by the FDTD method. In addition, Figure 6 shows a simplified image of Figure 5. This two-dimensional image is a cross-section of a human body at high 137.5 cm. This model contains human body tissues such as muscle, fat, blood, bone, stomach, intestine, bladder, tendon. As mentioned before, we consider four nodes at positions (171,61), (400,61), (171,240), and (400,240). On the other hand, there is one tag device. We simulate the proposed method within the region delimited by the four nodes.
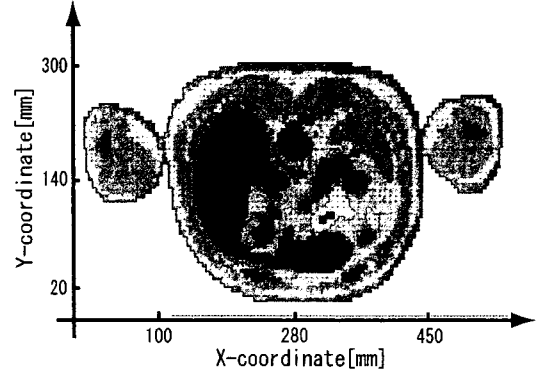

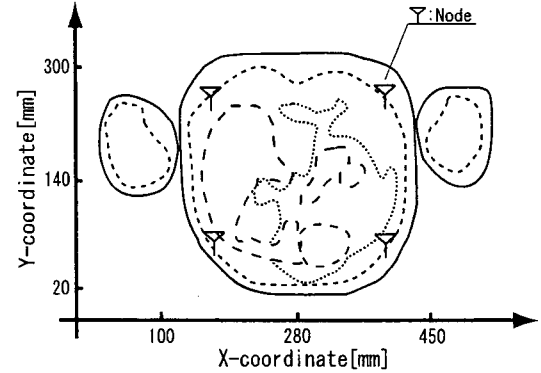Figure 5: 2D human body model of position of 137.5cm high of human body

Figure 6: Simplified 2D human body model of position of 137.5cm high

B. Bandwidth of UWB signal and accuracy of position estimation

Before we simulate the proposed method, we analyze the bandwidth of UWB signals and the accuracy of position estimation. Generally, as bandwidth of UWB signal becomes larger, ranging and position estimation accuracy are better, because a large bandwidth of UWB signal provides a high-resolution time. However, inside human body, the high-frequency components are attenuated. So, there is a limit in the accuracy of position estimation. We simulate a position estimation accuracy for several bandwidths of UWB signals. Figure 7

shows the simulation result. The horizontal axis shows a bandwidth of a UWB pulse and the vertical axis shows the RMSE of position estimation. In the Fig. 7, position estimation accuracy is better from 1 GHz bandwidth to 4 GHz bandwidth. However, over 4 GHz bandwidth, the position estimation accuracy remains the same, because received pulse is distorted by the attenuation of high-frequency components. Based on this result, we use UWB signals of 4 GHz bandwidth.
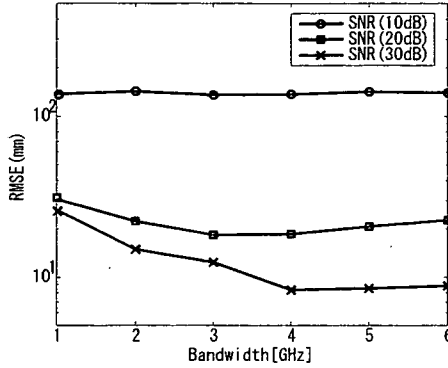

Figure 7: Relation between RMSE and bandwidth of UWB signal

C. Performance Evaluation of our proposed method

We evaluate the performance of our proposed method. At the second stage, we divide the large region inside of the four nodes into some smaller regions. The number of partitions is (3×3), (5×5), and (7×7) for x-direction and y-direction. We compare the proposal with the method using the average relative permittivity obtained in Table 1, in order to estimate the propagation velocity from all arbitrary tag points to a node point. The average relative permittivity inside the human body is assumed to be 2/3 of muscle and 1/3 of fat. The proportion of the tissue of high water content(HWC) to the low water content(LWC) is 2:1 in a human body, where the typical tissue of HWC is muscle and fat for LWC.

Transmit Waveform	Gaussian Mono Pulse
Used Band Frequency	$0 \sim 4.0$[GHz]
Time Step	1.926[ps]
Sequence	MLS(length=7)
Pulse Interval	5000[time steps]
Number of Time Step	40000
Kind of Noise	AWGN

Table 2: Simulation Specification

Figure 8 shows the result of position estimation. The horizontal axis shows SNR and the vertical axis shows RMSE of position estimation. Simulation results show that accuracy of proposed method of positioning is around the size of medical implanted device such as a capsule endoscopes. In addition,
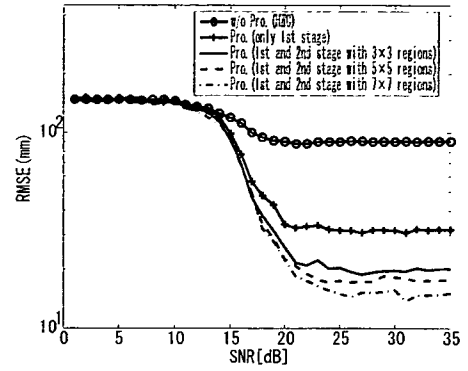

Figure 8: Comparison of positioning error

simulation results show that when the regions are smaller, the positioning accuracy is better.

VI. CONCLUSIONS

In this paper, we analyze the propagation of UWB signals inside of human body tissues with the FDTD method. Especially, we focused on the time-based position estimation of medical implanted devices inside human body using an estimation of the propagation velocity. Firstly, we analyze the relative permittivity of human homogeneous tissues. In addition, we analyze the relationship between the RMSE of position estimation and bandwidth of UWB signals. As a result, we show that UWB signals of 4 GHz bandwidth have a beneficial effect on the position estimation of medical implanted devices. Moreover, we have proposed the position estimation method of medical implanted devices using estimation of the propagation velocity inside of the human body. Simulation results show that the proposed method gives a positioning accuracy around the size of medical implanted devices such as capsule endoscopes. In addition, simulation results show that if the regions are smaller, the positioning accuracy is better. We estimate the propagation velocity inside human body without prior information of human body images.

REFERENCES

[1] Kazunari Tai, Hiroki Harada, Ryuji Kohno, "Channel Modeling and Signaling of Medical Implanted Communication Systems and a Step to Medical ICT," A3.5, IST Mobile Summit 2007, July 2007.

[2] Sinan Gezici, Zhi Tian, Georgios B.Giannakis, Hisashi Kobayashi, Andreas F.Molisch, H.Vincent Poor, and Zafer Sahinoglu, "Localization via Ultra Wideband Radios," IEEE SIGNAL PROCESSING MAGAGINE, pp70-84, Jul. 2005.

[3] Guilin Sun, Christopher W. Trueman, "Numerical Dispersion and Numerical Loss in Finite-Difference Time-domain Method in Lossy Media," IEEE Trans. Antennas Propag, vol.53 pp3684-3690, Nov 2005.

[4] Takeshi NAKAMURA, Masahiro SHIMIZU, Hiroshi KIMURA, and Risaburo SATO, "Effective Permittivity of Amorphous Mixed Materials," IEICE Trans.B, vol.J87-B No.11, pp.1951-1958, Nov.2004

医療用体内埋め込み装置の位置推定法に関する一検討
A Study on Position Estimation of Medical Implanted Devices

河嵜 誠　　　　田井 和成　　　　原田 浩樹　　　　河野 隆二
Makoto KAWASAKI　Kazunari TAI　Hiroki HARADA　Ryuji KOHNO

横浜国立大学大学院工学府物理情報工学専攻
Division of Electrical and Computer Engineering, Faculty of Engineering, Yokohama National University

1 はじめに

近年，医療用埋め込み装置の研究が行われている [1]．装置は低消費電力であることが望ましく，埋め込み機器相互の位置を把握することで，送信電力の最適化につながる．そこで，生体埋め込み機器の位置推定法について検討を行う．本稿では，体内組織の比誘電率の違いにより電磁波の伝搬速度が変化することから，電磁界解析手法である FDTD 法により比誘電率を推定し，求まる媒質内の伝搬速度を考慮した位置推定を行う．

2 埋め込み機器の位置推定法

位置推定を行う上で本稿では，低消費電力・高時間分解能を実現できる UWB 方式 [2] を採用する．自由空間における電波を用いた TOA 方式の位置推定では，電波の伝搬速度が光速で一定であることを利用し，受信波の到来時間を用いて位置推定を行う．しかし，生体内では各生体組織が比誘電率と導電率と呼ばれる電気定数を持ち，生体組織内での電波の伝搬速度は比誘電率 ε の関数で表される．従って，様々な臓器が混在する生体内では，埋め込み型通信装置の位置の違いにより伝搬速度が変化してしまうため，推定が困難である．

そこで本稿では，電磁界解析法である FDTD 法 (有限差分時間領域法) を用いることで，人体スライス画像内の様々な臓器の複雑構造を考慮した生体内の比誘電率の推定を行う．さらに，解析領域内での比誘電率の平均値を用いて伝搬速度を算出することで粗決定・精決定による二段階での位置推定を行う．ただし前提条件として，体内のスライス画像は事前に取得していることとする．粗決定・精決定方法について以下で述べる．

3 粗決定・精決定

粗決定・精決定により以下の手順で位置推定を行う．(以下では，位置が既知である装置をノード，未知である装置をセンサと呼ぶ)

1. 粗決定法
   - (1) センサ位置から各ノード間の実伝搬時間 $t_1 \sim t_4$ を FDTD 法により解析
   - (2) 解析領域内の任意の位置から各ノード間の推定伝搬時間を ε_{so} を用いて算出
   - (3) 各ノードにおける実伝搬時間と推定伝搬時間の時間差の総和が最小となる位置 (x,y) をセンサ粗決定位置と決定

2. 精決定法
   - (1) 粗決定領域を（5×5）の領域に分割
   - (2) それぞれの領域で ε の平均値を算出
   - (3) 各ノード・粗決定位置の間の伝搬経路の通過領域を判定
   - (4) 各ノードごとに粗決定位置に対する経路に応じた $\varepsilon_1 \sim \varepsilon_4$ を算出
   - (5) 解析領域内の任意の位置から各ノード間の伝搬時間を $\varepsilon_1 \sim \varepsilon_4$ を用いて算出
   - (6) 各ノードにおける実伝搬時間と推定伝搬時間の時間差の総和が最小となる位置 (x,y) をセンサ精決定位置と決定

4 性能評価

前述した方法により，粗決定および精決定による位置推定精度の性能評価をシミュレーションにより行った．ただし，今回は二次元人体モデルを使用し，ノード位置は図1のような配置であるとした．

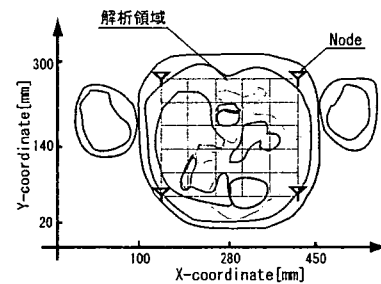| 使用モデル	XFDTD 人体モデル
使用波形	ガウシアンパルス
帯域幅	3GHz
解析領域	230 × 180[mm]

表 1　シミュレーション諸元

図 1　人体モデル
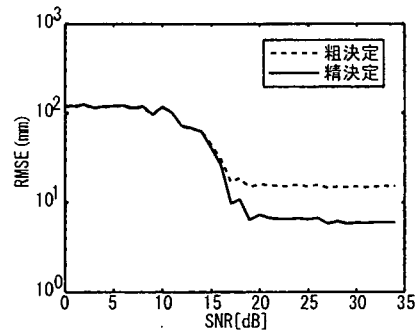

図 2　シミュレーション結果

図2の結果より精決定を行うことで位置推定精度を改善できていることがわかる．今回の検討では，ノード配置は固定とし，解析領域は1スライス画像として検討を行ったが，ノードの配置を変えた場合およびスライス画像を変えた場合の検討などが必要となる．

参考文献

[1] 杉町 勝,"ナノテクノロジーによる機能的・構造的生体代替デバイスの開発", 厚生労働省管轄

[2] 小林 岳彦, 幸谷 智,"UWB ワイヤレスシステムの研究開発動向," 電子情報通信学会論文誌 A, Vol.J86-A No.12 pp.1264-1273 Dec.2003

マッチング法を用いたインプラント位置推定法における
推定精度改善に関する検討
A Study on Improving Accuracy of Implant Position Estimation by Using Matching Method

田井和成   原田 浩樹   河野隆二

Kazunari TAI   Hiroki HARADA   Ryuji KOHNO

横浜国立大学大学院 工学府 物理情報工学専攻

Graduate School of Engineering, Yokohama National University

1 はじめに

近年，欧州や米国において，心臓ペースメーカーやカプセル型内視鏡といったインプラント機器が盛んに用いられている．このような中で，より高度な医療の実現の為に，体内または体外と無線通信することで，インプラント機器の制御や生体情報の受け渡しを可能にしたいという要求が高まってきている．ここで，インプラント機器間における通信電力を決定する際やこれら体内にあるインプラント機器の摘出時にインプラント機器の埋め込み位置を正確に知ることは重要である．そこで本稿では，マッチング法を用いて，インプラント機器の位置推定を行うことを提案する．さらに従来のマッチング法に受信アンテナ毎の重み付けを行うことで推定精度の改善を図る．

2 マッチング法を用いた推定方式

事前処理として体内データ (CT や MRI によるスライスデータ) から，仮想的な 3 次元人体モデルを計算機上で作成し，そこに平均的な体内電気定数を割りあてる．作成した人体モデルに格子点 T_{ij} を配置し，格子点上にインプラント機器と同じ送信信号を放射する送信点を置き，FDTD 法により体外アンテナでの受信波形を算出しテンプレート波形 r_{kij} として保存する．体内外での通信時において，実際の体内インプラント機器からの受信信号 $r_k(t)$ を得る．その後，式 (1) のように受信信号と各テンプレート波形で相関をとる．このとき，K は受信アンテナの本数，l は格子点の x 方向の個数，m は格子点の y 方向の個数，N はサンプル点の個数である．

$$Corr_k(i,j) = \max_\tau \left\{ \sum_{n=0}^N r_k(n) * r'_{kij}(n-\tau) \right\} \quad (1)$$

この評価関数 $Corr_{ij}$ において，最大値を与える $(i,j) = (i',j')$ の組を求め，それに対応する $T_{i',j'}$ をインプラント機器の位置と決定する．(i',j') について，式 (2) にて示す．また一連の処理を図 1 のフローチャートで示す．

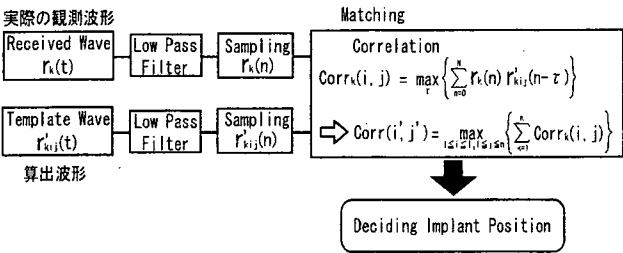$$Corr(i',j') = \max_{1 \le i \le l, 1 \le j \le m} \left\{ \sum_{k=1}^K Corr_k(i,j) \right\} \quad (2)$$

図 1 マッチング法を用いたインプラント法

図 2 にこの位置推定法によって得られた結果例を示す．ただし，ここでは，雑音の影響はなく体内組織構造およびその電気特性が既知であると仮定している．
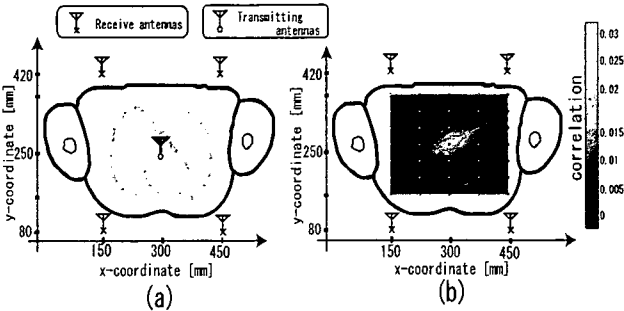

図 2 位置推定実行例

3 アンテナへの重み付けによる精度改善

これまではマッチング法を用いた位置推定をするときに，アンテナ毎の推定結果を平等に扱い位置推定を行った．しかし，インプラントから受信アンテナまでの距離を考えると，受信アンテナが送信位置に近い場合，雑音に対して受信電力はく，波形変化は小さくなる．一方で，受信アンテナが送信位置に対して遠い場合，波形の変化は大きく，また雑音電力に対して，受信電力は小さくなる．このことにより，単純に各アンテナでの相関値を合計した場合，送信位置が体表に近づくと推定精度が劣化する．よって図 3 のように各受信電力をパラメータとして用いた重み付けを行うことで推定精度の向上が見込まれる．
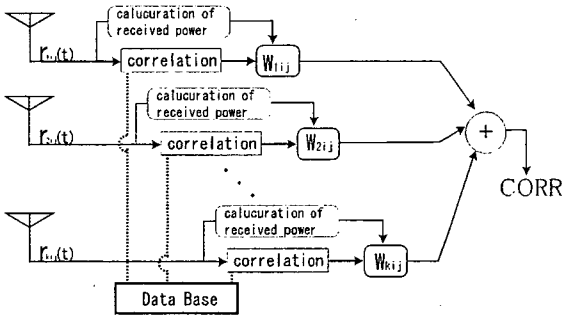

図 3 各アンテナへの重み付け例

4 まとめ

本研究では，マッチング法における SNR と波形変化に起因する推定精度のロバスト性を考慮し，各アンテナに対して重み付けを行った．このことにより，推定精度の向上が見込まれる．

参考文献

[1] 大森豊明，"バイオ電磁工学とその応用," 株式会社フジ・テクノシステム，Tokyo, pp. 14-29, 1992

[2] 菊池祥平，辻宏之，三浦龍，佐野昭，"マルチパス環境における周辺散乱モデルに基づく無線局の位置推定法," 信学論 (B) vol.J87-B No.12, pp.2020-2028, 2004 年 12 月．

生体内クラスタ型センサネットワークにおける熱影響を考慮した CSMA/CA の特性解析

Performance Analysis of CSMA/CA Considering Thermal Influence in a Clusterd Implant Sensor Network

長嶺 駿　　　　　原田 浩樹　　　　　河野 隆二
Shun Nagamiine　　Hiroki Harada　　Ryuji Kohno

横浜国立大学大学院 工学府 物理情報工学専攻
Graduate School of Engineering,Division of Physics,Electrical and Computer Engineering,Yokohama National University

1 はじめに

本稿では，生体内に埋め込まれたセンサ間の無線ネットワークにおける，人体への熱影響を抑圧するためのネットワーク構成について検討する．複数のセンサ端末によりクラスタを形成し，クラスタリーダとなる端末がセンサ端末の取得した生体情報を体外へまとめて送信するモデルを考える．この時，クラスタリーダ周辺は他のセンサ周辺よりも熱影響を受けやすい．そこで，本稿では熱を分散させるため，クラスタリーダの役割を 2 つの端末間で切り替える方式を提案し，細胞の上昇温度とリーダの切り替え間隔の関係について示す．また，アクセス制御方式として CSMA/CA を用いるときの，クラスタ内端末数とリーダが切り替わるまでの送受信回数の関係について，熱影響を考慮した上での解析を行う．

2 人体への安全基準と上昇温度の評価

生体内での上昇温度の時間特性は，熱輸送方程式と呼ばれる熱の伝搬を表す式を用いることによって算出することができる．電磁波によって生じた熱の生体内における伝搬現象の計算手法として一般的に用いられている以下の方程式 [2] により，上昇温度の評価を行った．

$$\rho C_p \frac{dT}{dt} = \kappa \nabla^2 T - \rho \rho_b C_b F (T - T_b) + \rho SAR \qquad (1)$$

ただし，$\rho(\rho_b)$: 生体組織 (血液) の密度 $[kg/m^3]$, $C(C_b)$: 生体組織 (血液) の比熱 $[J/kgK]$, κ : 生体組織の熱伝導率 $[W/mK]$, $T(T_b)$: 生体組織 (血液) の温度 $[℃]$, F : 血液の流量率 $[m^3/kgs]$ である．

今回のモデルでは，最も熱影響を受けやすい筋肉組織での評価を行った．従って筋肉における上昇温度が安全な範囲内で通信を行うことを条件とした．安全とみなす基準であるが，本稿では温度という観点から評価することにする．ここで，全身または一部の 1 度以上の加温により身体に影響を及ぼすという実際にあった報告 [1] を根拠に，上昇温度の規制値 T_{lim} としてその値に安全率 50 倍をかけた 0.02 ℃を設けた．

3 切替間隔と上昇温度の関係

リーダとなる端末の電力消費を抑える事は，ネットワーク全体の長寿命化に繋がる．そこで，2 つの端末間でリーダとしての役割を等間隔で切り替えることにより，電力消費と熱影響を分散させる方式を提案する．

ここに切り替え間隔と，そのときの細胞の飽和温度の関係を (1) 式を用いて求めた (図 1)．温度の評価はリーダの地点のみとし，給電電力は 0.5[mW]，電波は 2.45[GHz] の正弦波とした．また，簡略化のため，リーダ期間中は一定の電力と考える．

4 CSMA/CA 特性解析

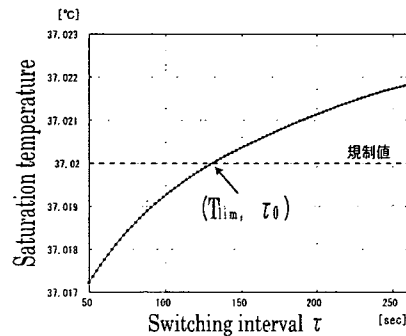図 1 より，ある飽和温度となる切り替え間隔は一意に求まる．熱的に安全な範囲内での通信は，図中の τ_0 を超えない間隔でリーダを切り替えればよいことが言える．そこでクラスタ
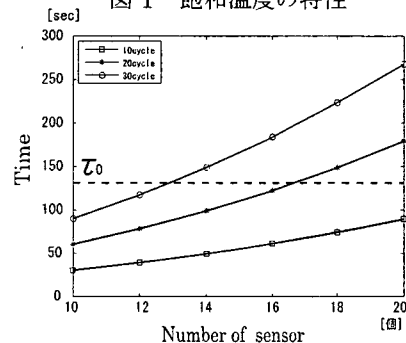

図 1　飽和温度の特性

図 2　CAMA/CA 方式における処理時間特性

内における情報収集のアクセス方式が CSMA/CA 方式であった場合に，クラスタ内端末数と，処理時間について，T_{lim} を超えない範囲での設定を計算機シミュレーションによって検討した．なお，MAC 層におけるフレーム長などの各パラメータは IEEE802.15.4 の規格を基準にした．1cycle はリーダの 1 回分の受信＋送信を指し，一定の cycle を経過したらリーダを切り替えると考える．図 2 より，端末数に対応したリーダ切り替えまでの cycle 数の目安を設計することができる．

5 今後の検討について

今後の検討としては，熱影響をリーダの送受信状態や回路熱などに分けて定式化することで，より温度上昇を抑える通信状態をとるような MAC プロトコルの検討を行い，定量的に評価する必要がある．

参考文献

[1] 国際非電離放射線防護委員会"時間変化する電界，磁界及び電磁界による曝露を制限するためのガイドライン (300GHz まで)"1984 年 4 月

[2] 久世直樹, 石橋功至, 松田慧, 原田浩樹, 河野隆二"生態の温度上昇評価による体内無線通信方式の検討"信学技法 RCS2005-228,pp.301-305,May.2006

生体内センサーネットワークにおける位置推定法の検討

河嵜 誠　田井 和成　原田 浩樹　河野 隆二

横浜国立大学大学院　工学府　物理情報工学専攻

A Study on Position Estimation in an Implanted Sensor Network

KAWASAKI MAKOTO TAI KAZUNARI HARADA HIROKI KOHNO RYUJI

Division of Physics, Electrical and Computer Engineering, Graduate School of Engineering, Yokohama National University

Recently, wireless communication devices in the field of medical implant, such as cardiac pacemakers and capsule endoscopes, have been studied and developed to improve healthcare systems. Especially it is very important to know a range and a position of each device because it will contribute to optimization of transmission power. We adopt the time-based approach of a position estimation using UWB (Ultra Wideband) signals. However, radio propagation velocity inside of the human body differs in each homogenous tissue. In this paper, we propose the position estimation method using an estimation of a propagation velocity inside of the human body. In addition, we show by computer simulation that the proposed method can perform accurate positioning with the size of medical implanted devices such as capsule endoscopes.

Keywords: positioning, inside human body, UWB, relative permittivity, propagation velocity

1. はじめに

近年,医療において心臓ペースメーカやカプセル型内視鏡などの医療用埋め込み通信装置の研究が行われ実用化が進められている。将来的には複数の小型の通信装置を埋め込みネットワークを形成し,相互無線通信を行い生体情報を得ることで健康状態を常に把握し,同時に治療も行うことが目指されている.[1]

埋め込み装置における無線通信を考えたとき,生体情報を扱うことを考慮すると信頼性の高い通信が要求される.さらに,装置のバッテリー電力を考慮すると低消費電力であることが必要となる.そのため,埋め込み機器相互の距離・位置を把握することが,送信電力の最適化につながり,非常に重要である.そこでこれらの要求をふまえ,本研究では生体内における埋め込み型機器相互の距離推定および位置推定について検討を行う.

自由空間における電波を用いた位置推定法の一つに,電波の伝搬速度が光速で一定であることを利用し,受信波の到来時間から位置推定を行う方法がある.超広帯域(UWB)信号は,時間分解能が高く,この位置推定方式に適していると考えられる.しかし,生体内では各生体組織が比誘電率と導電率と呼ばれる電気定数を持ち,生体組織内での電波の伝搬速度は比誘電率の関数で表される.従って,様々な臓器が混在する生体内では,埋め込み型通信装置の位置の違いにより伝搬速度が変化してしまうため,推定が困難である.

そこで本研究では,生体内センサーネットワークにおいて生体内の比誘電率分布を考慮することで体内における伝搬速度を推定し,推定伝搬速度を用いた埋め込み通信装置の位置推定法を提案する.事前にMRIやCTなどを用いて生体内画像は得られており,組織分布は既知であるとする.そこで,UWB帯域幅と位置推定精度について評価を行い,さらに提案方式における位置推定精度について評価を行う.

2. UWBを用いた位置推定法

複数のセンサが存在するようなセンサーネットワークにおいて,位置が既知であるセンサ(以下,ノードと呼ぶ)と位置が未知であるセンサ(以下,タグと呼ぶ)の間の位置推定法には,到来方向(Angle of arrival; AOA),受信電力(Signal strength;SS),ノード・タグ間の伝搬時間に基づいた方法がある.AOAでは,複数のノードとタグ間の電波の到来角を測定することで位置推定を行う.一方,SSはノードにおいてタグから電波の受信電力を測定することで,また伝搬時間による方法では,タグからの電波の到来時間を測定することでそれぞれ位置推定を行う.

特にUWBを用いた場合には,伝搬時間に基づく方法が高精度を達成することが出来る.これは,UWB信号が超広帯域幅を有することによる時間分解能が高いという特徴を活かせるためである.伝搬時間に基づく方法には,TOA(Time-of-arrival)方式とTDOA(Time-difference-of-arrival)方式の2種類が主に挙げられる.伝搬時間の測定には,ノード側における相関器においてあらかじめ用意されているテンプレート波形と受信信号との相関を取ることで,その相関出力により伝搬時間の決定を行う.さらに,TOA方式による最小二乗法に基づく位置推定法もある.そこで本論文では,TOA方式に基づく最小自乗法により位置推定を行う.[2]

3. 生体内伝搬特性

3.1 生体組織の電気定数・電気特性

生体は,さまざまな臓器によって複雑な構造をなして構成されている.さらに,各臓器は比誘電率,導電率と呼ばれる電気定数を持っており,それら定数は周波数特性を有する.

広帯域幅を有するUWB信号を用いて,埋め込み型装置の通信および位置推定を行う場合には,これら電気定数の周波数特性を考慮することが必要となってくる.生体のような電気定数が周波数特性を有する分散性媒質における電気定数は一般的にCole-Coleモデ

ルで与えられている.[1]

$$\varepsilon_r(\omega) = \varepsilon_\infty + \sum_{n=1}^{4} \frac{\Delta\varepsilon_n}{1+(j\omega\tau_n)^{1-\alpha_n}} + \frac{\sigma}{j\omega\varepsilon_0} \qquad (1)$$

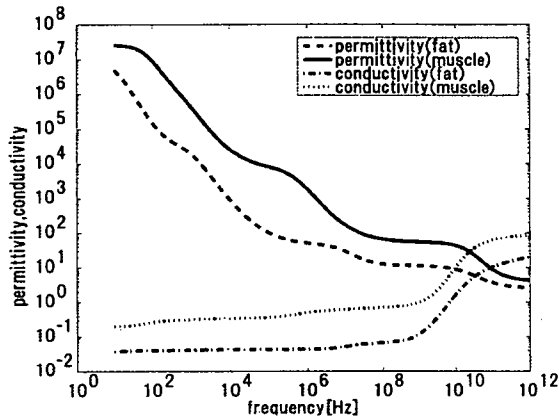式(1)のCole-Coleの式より導出される比誘電率・導電率の周波数特性は図1のようになる.図1は筋肉・脂肪のグラフである.

図1 比誘電率・導電率の周波数特性

さらに,媒質中の伝搬速度は式(2)で表され,比誘電率の関数で表されることが知られている.そのため,生体内においては,伝搬速度は各臓器および周波数によって異なることが分かる.ここで,cは光速,ωは角周波数を表している.

$$v(\omega) = \frac{c}{\sqrt{\varepsilon_r(\omega)}} \qquad (2)$$

4. 提案位置推定法

4.1 均一媒質における比誘電率

図1のように比誘電率は周波数特性を持っているが,相関器出力より得られる到来時間を,式(2)より導出される以下の式(3)に代入することで比誘電率を一意に算出できる.そこで,本論文ではFDTD法[3]を用いて均一媒質における比誘電率(伝搬速度)の解析を行った.ここで,tは到来時間,dは伝搬距離を表している.

$$\varepsilon_r = \left(\frac{c\times t}{d}\right)^2 \qquad (3)$$

表1 各媒質の平均比誘電率

Tissue	muscle	fat	blood	intestine
ε_r	47.83	4.08	51.59	50.67
Tissue	stomach	bone	tendon	bladder
ε_r	56.99	17.09	37.61	64.63

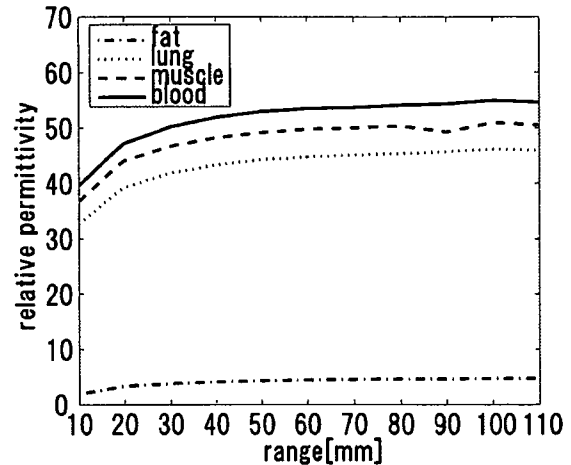その結果,図2のように比誘電率は距離特性を持っていることが分かり,さらに,本論文ではそれらの値の平均値を求めることで各媒質ごとの比誘電率を一意に決定した.表1は各媒質ごとの比誘電率の平均値を示したものである.

図2 均一媒質の比誘電率

4.2 位置推定法

本論文では,生体内における電波の伝搬速度を推定することにより,埋め込み機器の位置推定を行う.

提案方式の前提条件として2つの条件を設定している.まず,MRIやCTなどを用いて生体内の画像は得られている(組織分布が既知である).さらに,位置が既知である埋め込み機器が4つ存在していることである.生体内は各臓器が複雑に混在しているため,伝搬速度を全ての経路において推定することは困難である.そこで,本論文では伝搬速度を段階的に推定していき位置推定を行う.提案位置推定法は以下の2つの段階で構成されている.

4.2.1 第一段階

1段階目として,得られた生体画像内において,4つのノードの内部領域(解析領域)の平均的な比誘電率を以下の式(4)より算出する.ここで,εは比誘電率,pは各組織の分布割合,Iは組織数を表している.また図3は1段階目のシステムモデルを示している.

$$\varepsilon_{ave} = \sum_{i=1}^{I} (\varepsilon_{I(i)} \times p_{I(i)}) \qquad (4)$$

得られた平均比誘電率より、平均的な伝搬速度を以下の式(5)より算出する。

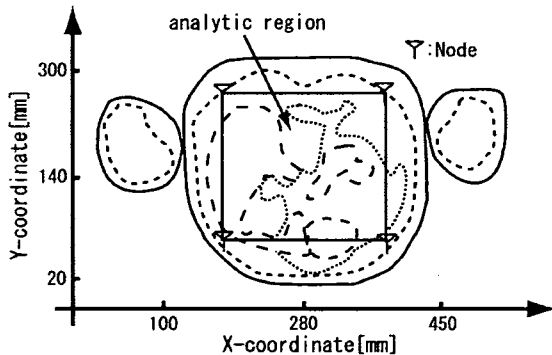$$v_{ave} = \frac{c}{\sqrt{\varepsilon_{ave}}} \qquad (5)$$

図3 システムモデル(第一段階)

図4 システムモデル(第二段階)

ここで、生体内画像内の全ての任意点(x,y)から各ノードまでの伝搬時間を式(5)より求められたノードごとの伝搬速度および各ノードから任意点までの距離を用いて、式(6)より算出する.ここで,nはノード番号,dnは任意点から各ノードまでの距離を表している.

$$t_{n(x,y)} = \frac{d_{n(x,y)}}{v_{ave}} \qquad (6)$$

そして,式(6)により求められた伝搬時間とFDTD法を用いて実際に得られるノード・タグ間の伝搬時間との最小自乗誤差を得る位置を推定位置と決定する.[2]

$$\theta(x,y) = \min\sum_{n=1}^{4}[t_n - t_{n(x,y)}]^2 \qquad (7)$$

4.2.2 第二段階

2段階目では,1段階目で得られた推定位置を用いてさらに,精度を向上させるために位置推定を行う.手順は以下のようになっている.

まず,得られた生体内画像を複数領域に分割する.領域内に存在する媒質の比誘電率 ε およびその割合pをもとに式(8)より領域ごとの比誘電率を算出する.図4は分割数(3×3)の場合のシステムモデルを示している.jは図4における領域番号を示している.

$$\varepsilon_j = \sum_{i=1}^{I}\left(\varepsilon_{t(i)} \times p_{t(i)}\right) \qquad (8)$$

さらに,1段階目で得られた推定位置とノード間の経路が通過する領域および通過距離を算出することで,式(9)より推定位置・ノード間の比誘電率を算出する.kは図4における通過領域番号を示している.

$$\varepsilon_n = \frac{\sum_{k=1}^{K}\left(\varepsilon_k \times d_k\right)}{d_{all}} \qquad (9)$$

この比誘電率を用いて各ノードごとに伝搬速度を算出し,1段階目の式(7)と同様にして最小自乗法により位置推定を行う.
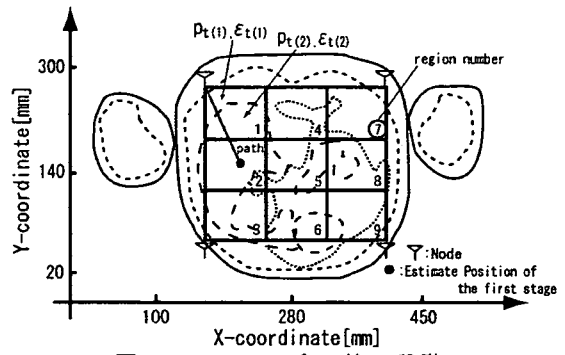
5. 計算機シミュレーションによる性能評価

この章では、提案方式のシミュレーションによる性能評価および結果について述べる。

5.1 シミュレーションモデル

シミュレーションモデルは図5のようになっている.この図は成人男性の高さ137.5cmにおける腹部のモデルであり,筋肉,脂肪,血液,骨,胃,小腸,胆のうなどの臓器が含まれている.ノード位置はそれぞれ(171,61),(400,61),(171,240),(400,240)と設定し,タグの存在領域は4つのノードの内部領域(x=171〜400[mm],y=61〜240[mm])とした.
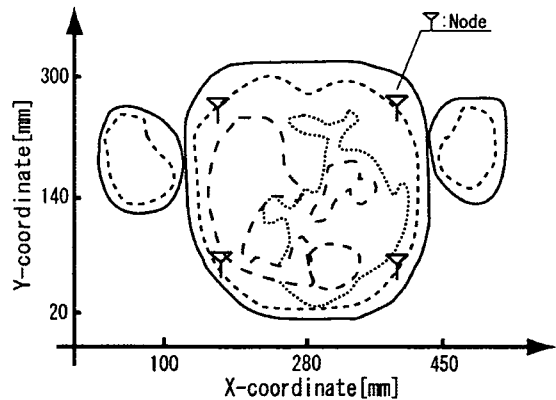

図5 シミュレーションモデル

5.2 UWB帯域幅と位置推定精度評価

提案方式の性能評価を行う前に,UWB信号の帯域幅と位置推定精度の解析を行った.

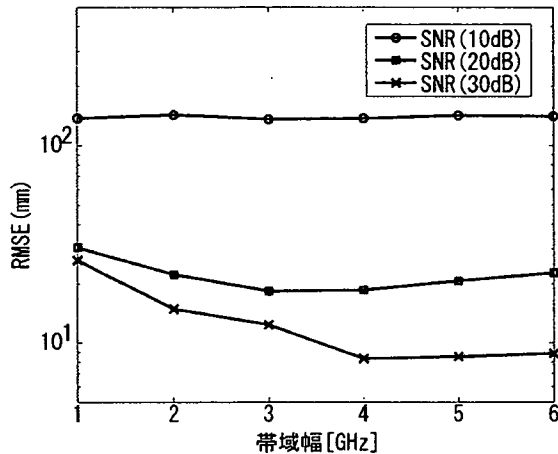一般的には,帯域幅が広がると位置推定精度は向上する.しかし生体内においては,高周波数成分が激しく減衰してしまうため,位置推定精度に限界が存在する.

図6 UWB帯域幅と位置推定精度

そこで,シミュレーションにより送信UWB信号帯域幅と位置推定精度の関係をシミュレーションにより解析した.結果は図6のようになっている.横軸はUWB信号の帯域幅,縦軸は位置推定誤差を表している.この結果より,雑音が信号に対して小さい場合には帯域幅が1[GHz]から4[GHz]にかけて位置推定精度がよくなっていることがわかる.しかし,帯域幅が4[GHz]以上になると推定精度が向上していない.これは,生体内において高周波成分が減衰してしまい,精度が上がらないためである.そこで,提案方式の解析には0~4[GHz]帯のUWB信号を用いて性能評価を行う.

5.3 提案位置推定法の性能評価

次に提案方式の性能評価を行った.2段階目の分割領域数を(3×3),(5×5),(7×7)として行った.生体組織の比誘電率として高含水組織(HWC)の比誘電率を用いた場合との比較を行った.高含水組織は含水量の高い組織の総称であり,生体組織の約3分の2を占めるもので,組織の代表としては筋肉などが挙げられる.高含水組織の比誘電率の値として,表1の筋肉の値の3分の2の値を用いた.

表2 シミュレーション諸元

送信波形	ガウシアンモノパルス
使用帯域	0~4[GHz]
サンプリング間隔	1.926[ps]
パルス間隔	5000×1.926[ps]
使用系列	M系列(系列長=7)
雑音	AWGN

結果は図7のようになっている.横軸に受信信号電力対雑音電力比(SNR),縦軸に位置推定誤差を示している.シミュレーション結果より,高含水組織の平均の比誘電率を用いた場合と比べて,提案方式においては,精度が向上できていることがわかる.さらに既存のカプセル型内視鏡などの大きさ20[mm]ほどの分解

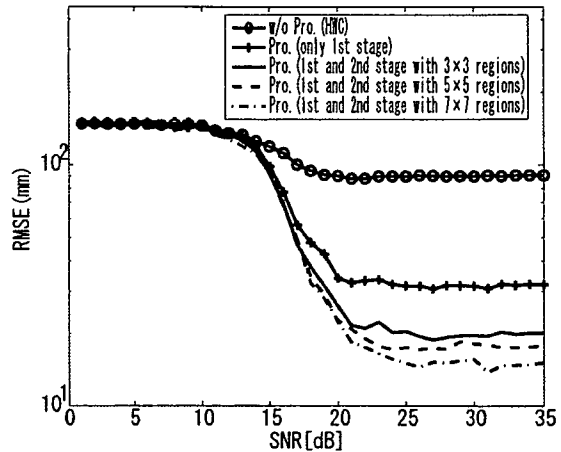能を達成できていることがわかる.また,分割領域数を細かくすることで,精度を向上できることを示した.

図7 提案方式による位置推定精度

6. むすび

本論文では,生体内の伝搬速度の推定による医療用埋め込み型機器の位置推定法を提案した.生体内においてUWB信号のような広帯域信号を用いる場合には,位置推定精度に高周波成分の減衰が大きく影響してくるが,0~4[GHz]帯のUWB信号を用いた位置推定による精度が他の帯域幅を用いた場合に比べ精度が良いことを示した.さらに,高含水組織の比誘電率の平均値を用いて伝搬速度を算出した場合と比べて,提案方式において伝搬速度を推定することで,推定精度を大きく改善できることを示した.さらに提案方式では,既存のカプセル型内視鏡などの大きさ20[mm]ほどの分解能が得られることを示した.

今後の課題としては,事前情報によらない位置推定法の検討および実験による提案方式の実践などが挙げられる.

参考文献

[1] kazunari Tai, Hiroki Harada, Ryuji Kohno, ."Channel Modeling and Signaling of Medical Implanted Communication Systems and a step to Medical ICT, ".A3.5, IST Mobile summit 2007. July 2007.

[2] Sinan Gezici, Zhi Tian, Georgios B.Giannakis, Hisashi Kobayashi, Andreas F.Molisch, H.Vincent Poor, and Zafer Sahinoglu,."Localization via Ultra wideband Radios".IEEE SIGNAL PROCESSING MAGAZINE, pp70-84, Jul 2005.

[3] Guilin Sun, Christopher W.Trueman."Numerical Dispersion and Numerical Loss in Finite-Difference Time-Domain Method in Lossy Media".IEEE Trans, Antennas Propag, Vol.53, pp3684-3690, Nov 2005.

[4] 中村 隆, 清水 雅彦, 木村 宏, 佐藤 利三郎,."不定形混合媒質の実効誘電率".電子情報通信学会論文誌 B, Vol. J87-B, No.11, pp1951-1958, Nov 2004.

THE PERFORMANCES OF AN ENZYME-BASED MICROFLUIDIC BIOFUEL CELLS USING VITAMIN K$_3$-MEDIATED GLUCOSE OXIDATION

M. Togo, A. Takamura, T. Asai, H. Kaji, T. Abe and M. Nishizawa
Department of Bioengineering and Robotics, Graduate School of Engineering,
Tohoku University, Sendai 980-8579, Japan

ABSTRACT

This paper reports performances of an enzyme-based microfluidic biofuel cell under several controlled flow conditions. A reference and counter electrode-containing microfluidic biofuel cell enables to evaluation an individual performance of anode and cathode, separately. By using this system, we studied the optimum design of microfluidic biofuel cell.

Keywords: biofuel cell, enzyme, vitamin K$_3$, microfluidics

1. INTRODUCTION

Enzyme-based biofuel cells would be formatted into microfluidic systems as power sources for independent power-on-chip and implantable devices because such cells can have a simple structural design (non-compartmentalized) and can operate under mild conditions. Such systems are also useful when evaluating the electrochemical stability or activity of an experimental biofuel cell, because the fuel flow rate, which can affect the cell's performance, can be regulated. We, therefore, constructed a microfluidic-type biofuel cell system containing an Ag|AgCl reference electrode and a Pt counter electrode.
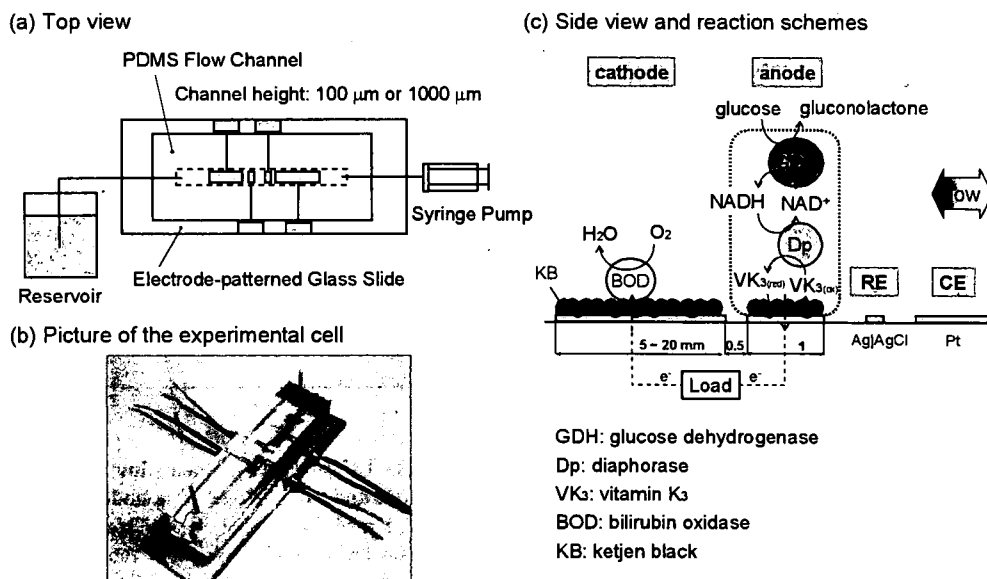

Figure 1. Schematic illustration(a), picture (b) and reaction schemes(c) of microfluidic biofuel cell.

2. EXPERIMENTAL

A schematic illustration and a picture of the present microfluidic biofuel cell are shown in Figure 1. Because this experimental system is equipped with an Ag|AgCl reference electrode and a Pt counter electrode in addition to glucose anode and an O_2 cathode, we can evaluate electrochemical reaction of an anode and a cathode separately as well as total cell performance. Figure 1(c) shows reaction scheme of the enzyme-catalyzed glucose oxidation[1, 2] and O_2 reduction at anode and cathode electrodes. By using vitamin K_3 as an electron mediator, our fuel cell becomes harmless for environment.

3. RESULTS AND DISCUSSION

Figure 2 shows the current density of O_2 reduction at enzyme cathodes (poised at 0V vs. Ag|AgCl) as a function of electrode area, studied in 1000 μm and 100 μm height fluidic channels. The O_2 reduction current density decreased with increasing electrode area and with decreasing the channel height probably due to the growth of O_2 depletion zone comparable to the channel height. It is suggested, however, that the "fuel utilization" can be improved in a narrower microchannel. Figure 3 shows the cell and electrode performance with different positioning of electrodes: the upstream cathode (●) and downstream cathode (□). As described above, our microfluidic biofuel cell system contains reference electrode and counter electrode, we can evaluate performance of anode and cathode, separately. At higher current region (> 20 μA), the current of biofuel cell with upstream cathode was higher than that with downstream cathode. The analogy in V-I shapes of the biofuel cell and the anode indicates the anode reaction kinetically limits the total performance of the cell. The upstream cathode reaction eliminated O_2, that slightly oxidize the anode constituents from the vicinity of downstream anode, and improved anode's and total cell's performances.
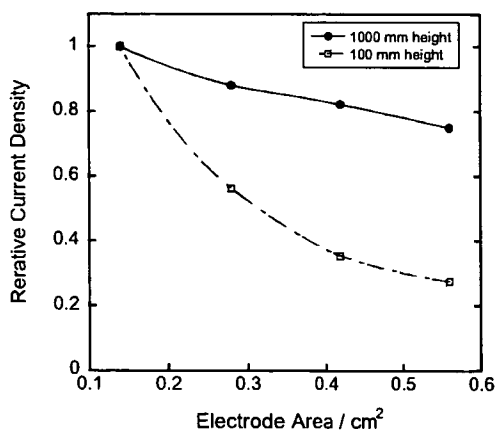

Figure 2. O_2 reduction current density versus electrode area (electrode length) with channel height of 1000 μm or 100 μm. The 0.1 M NaCl containing-phosphate buffer (pH 7) at room temperature was flowed at 10 cm min⁻¹.
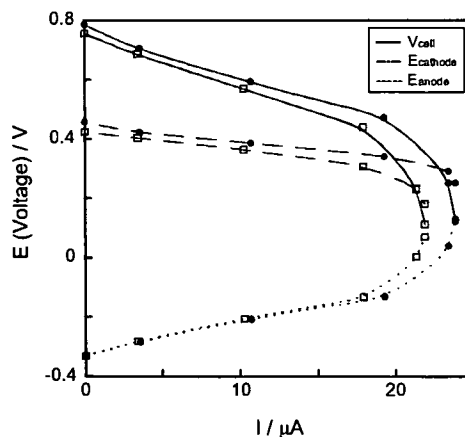

Figure 3. E(V)-I curve of microfluidic biofuel cell, anode and cathode operating under 10 mM glucose 1 mM NAD^+, 0.1 M NaCl containing phosphate buffer (pH 7) at room temperature, with a flow rate of 10 cm min⁻¹. Chennel height: 1000 μm. Upstream cathode (●) and downstream cathode (□).

Figure 4 shows the illustration and the performance of microfluidic biofuel cells constructed by sandwiching a silicone spacer of 100 µm or 1000 µm thickness between two electrode-patterned glass slides. Operation with the 100 µm-height channel (▲) shows smaller cell current and power than those with the 1000 µm-height channel (●) because of depletion of fuel in the narrower flow channel. The maximum cell current (I_{max}) of the 1000 µm-height cell (44 µA) was almost twice of that shown in Figure 3(●) (24 µA), corresponding to the increased electrode area. Although the I_{max} in 100 µm-height channel didn't become double due to the influence of highly developed depletion zone, the volume density of the current and power obtained in a 100 µm height channel was bigger than that in a 1000 µm-height channel (data not shown).
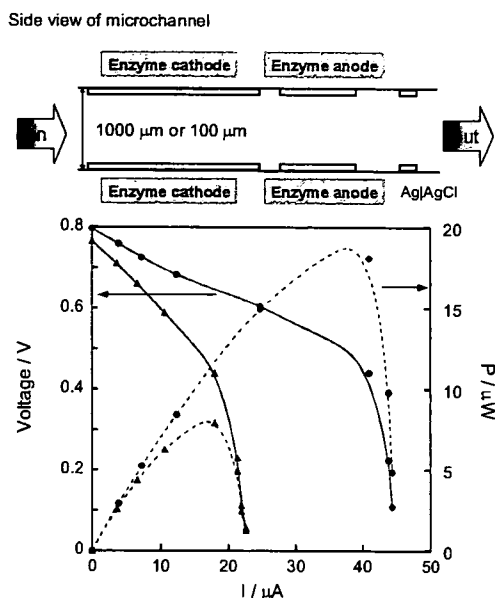
Side view of microchannel

Figure 4. Schematic illustration (top) and performance (bottom) of microfluidic biofuel cell operating under 10 mM glucose, 1 mM NAD^+, 0.1 M NaCl-containing phosphate buffer (pH 7) at room temperature, with a flow rate of 10 cm min^{-1}. Channel height: 100 µm (▲) and 1000 µm (●).

4. CONCLUSIONS

We assembled a microfluidic biofuel cell equipped with reference and counter electrode to evaluate the anode's and cathode's performances individually. It is important to consider depletion zone of fuel and oxidant in order to develop a high performance microfluidic biofuel cell. The depletion zone was easily developed within a microfluidic channel, and thus the prereduction of O_2 by upstream cathode can improve anode performance. Also, the power density and fuel utilization was higher in case narrower channel.

ACKNOWLEDGEMENTS

REFERENCES

[1] M. Togo, A. Takamura, T. Asai, H. Kaji, M. Nishizawa, Electrochim. Acta, 52 (2007) 4669.
[2] F. Sato, M. Togo, M.K. Islam, T. Matsue, J. Kosuge, N. Fukasaku, S. Kurosawa, M. Nishizawa, Electrochem. Commun., 7 (2005) 643.

Eleventh International Conference on Miniaturized Systems for Chemistry and Life Sciences
7 – 11 October 2007, Paris, FRANCE

870

ELSEVIER

JOURNAL OF
POWER
SOURCES

Short communication

Structural studies of enzyme-based microfluidic biofuel cells

Makoto Togo, Akimasa Takamura, Tatsuya Asai,
Hirokazu Kaji, Matsuhiko Nishizawa*

*Department of Bioengineering and Robotics, Graduate School of Engineering, Tohoku University, Aoba 6-6-01,
Aramaki, Aoba-ku, Sendai, Miyagi 980-8579, Japan*

Abstract

An enzyme-based glucose/O_2 biofuel cell was constructed within a microfluidic channel to study the influence of electrode configuration and fluidic channel height on cell performance. The cell was composed of a bilirubin oxidase (BOD)-adsorbed O_2 cathode and a glucose anode prepared by co-immobilization of glucose dehydrogenase (GDH), diaphorase (Dp) and VK_3-pendant poly-L-lysine. The consumption of O_2 at the upstream cathode protected the downstream anode from interfering O_2 molecules, and consequently improved the cell performance (maximum cell current) ca. 10% for the present cell. The cell performance was also affected by the channel height. The output current and power of a 0.1 mm-height cell was significantly less than those of a 1 mm-height cell because of the depletion of O_2, as determined by the shape of the E–I curve at the cathode. On the other hand, the volume density of current and power was several times higher for the narrower cell.
© 2007 Elsevier B.V. All rights reserved.

Keywords: Biofuel cell; Vitamin K_3; Diaphorase; Glucose dehydrogenase; Microfluidics

1. Introduction

Various kinds of miniature devices for ubiquitous power supplies have been developed in recent years [1–5]. The enzymatic biofuel cell is one option for such a device because it works under mild conditions: room temperature, neutral pH and atmospheric pressure [6–21] that increase freedom of construction including miniaturization. The enzymatic biofuel cells are composed of a couple; an anode and cathode, modified with an enzyme catalyst and usually an electron transfer mediator, and they generate electric power from an aerobic solution containing biofuel such as glucose. The dissolved molecular O_2 is the substrate of the cathodic enzyme reaction and also acts as the interfering substance for anode reactions. It is experimentally known that the dissolved O_2 can intercept electrons from the anode (enzymes and/or mediators) and consequently lower the externally delivered power. For example, Heller's group has reported that the power density of their biofuel cell in O_2-saturated solution was 30% lower than that in air because of the undesirable electron transfer from glucose oxidase (GOD) to the dissolved

O_2 [22–25]. Also, we have studied a glucose anode prepared by co-immobilization of enzymes and vitamin K_3 (VK_3) as an electron mediator [6,9], and reported lower performance in the aerobic solution [6] probably caused by leakage of electrons from enzymes and VK_3 to O_2 molecules. In addition to these energy losses due to reversible reaction with O_2, irreversible oxidative degradation of mediators and enzymes could become serious during longer periods of operation [26]. The simple answer to address these unfavorable reactions of O_2 at the anode is to compartmentize the deoxygenized anode room and oxygenized cathode room by a separator [17] or laminar flow [7]. Such complicated systems, however, may not be suitable to miniature power sources. In contrast, we have another choice to decrease the O_2 flux to the enzymatic anode and that is by electrode-arrangement in the single flow channel. The upstream cathode may deplete O_2 from the vicinity of the downstream anode within a microfluidic channel.

In the work reported in this paper, we constructed an enzyme-based microfluidic biofuel cell composed of a bilirubin oxidase (BOD)-adsorbed O_2 cathode and a glucose anode prepared by co-immobilization of glucose dehydrogenase (GDH), diaphorase (Dp) and VK_3-pendant poly-L-lysine. We studied the effects of pre-electrolysis of O_2 at the upstream cathode on the performance of the downstream anode both experimentally and

---

* Corresponding author. Tel.: +81 22 217 7003; fax: +81 22 217 3586.
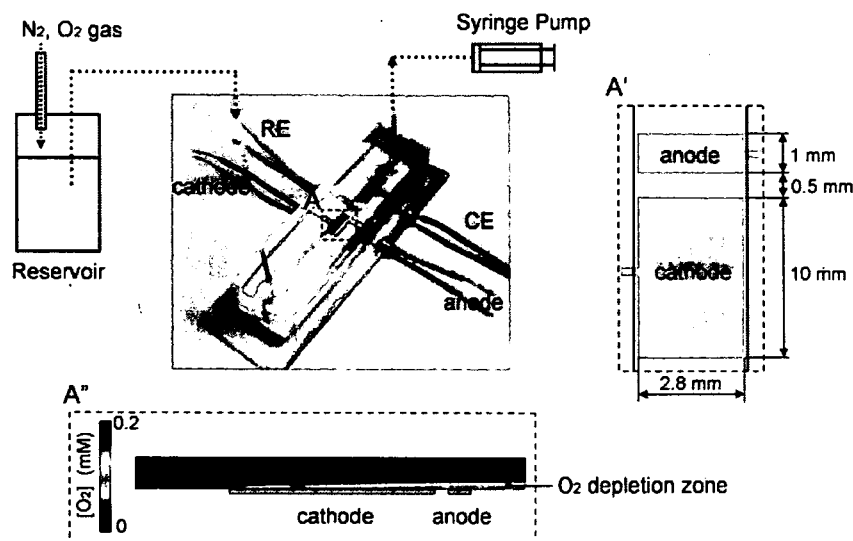 *E-mail address:* nishizawa@biomems.mech.tohoku.ac.jp (M. Nishizawa).

Fig. 1. Schematic illustration and photograph of microfluidic biofuel cell with (A′) the close up top view of the electrodes and (A″) the cross-sectional view of a COMSOL simulation of an O_2 depletion layer forming along the channel.

theoretically under regulated conditions: flow velocity, electrode length, electrode gap and channel height. Based on the results obtained, the optimum design of a fluidic cell will be discussed from the aspects of power and power density.

2. Experimental

2.1. Reagents

The synthesis of the redox polymer VK$_3$-modified poly-L-lysine (PLL-VK$_3$) has been described previously [6]. The diaphorase (Dp) from Bacillus stearothermophilus (EC 1.6.99, 1090 U mg^{-1}) was purchased from Unitika. NAD$^+$-dependent glucose dehydrogenase (GDH; EC 1.1.1.47, 250 U mg^{-1}) was donated by TOYOBO. Bilirubin oxidase (BOD) from Myrothecium sp. (EC 1.3.3.5, 2.45 U mg^{-1}) was purchased from Amano Enzyme Inc. Ketjenblack (KB; EC-600JD) was supplied by Ketjen Black International, Inc. NAD$^+$ was used as received from Oriental Yeast Co.

2.2. Electrodes preparation

A PLL-VK$_3$/Dp/GDH-coated KB electrode was prepared as previously reported [6]. A brief description of the preparation follows. Unless otherwise indicated, the enzyme solutions for electrode modification were prepared using 50 mM phosphate buffered solution (pH 7.0). An 8 μL PLL-VK$_3$ solution (4.83 mM VK$_3$) was mixed with a 2 μL Dp solution (14 μg μL^{-1}) and 1 μL of KB dispersed water (ca. 13 mg mL^{-1}). A 5.3 μL portion of the resulting solution was put onto a gold film electrode (surface area, 0.028 cm^2) on a glass substrate, and was left to dry in air. To create the enzymatic bilayer, the surface of a PLL-VK$_3$/Dp-coated KB electrode was coated with 1.6 μL of a solution composed of equal volumes of a 16 μg μL^{-1} GDH solution and a 16 mg mL^{-1} PLL solution.

A BOD-adsorbed KB electrode was prepared as described below. A mixture of 3:1 weight ratio of KB and poly(tetrafluoroethylene) (MW 5000–20,000, Wako) was dispersed in isopropanol (2 mg mL^{-1}), and applied to a gold electrode (0.11 mL cm^{-2}) followed by overnight drying in a 70 °C oven. And then, BOD was adsorbed to the KB electrode by dipping in the 5 mg mL^{-1} BOD solution for 10 min and washed with phosphate buffer solution for 10 min. The measurement was carried out before the BOD-modified electrode dried completely because the BOD loses its activity in the dry state [27,28].

2.3. Microfluidic biofuel cell and electrochemical measurements

We constructed microfluidic fuel cells of the type shown in Fig. 1. Film electrodes were patterned on the surfaces of glass slides by photolithography and spattering, which is a lift-off process. Both anode's (2.8 mm width, 1 mm long) and cathode's (2.8 mm width, 10 mm long) Au current collectors were modified by KB and enzymes. The gap between anode and cathode was 0.5 mm. The Ag|AgCl electrode was fabricated by coating a Pt film with Ag|AgCl ink (BAS Inc.) that was then cured at 80 °C for 2 h. A negative of the channel shape was prepared by thick photoresist (SU-8 2050, Microchem) by photolithography and transcribed to polydimethylsiloxane (PDMS; SYLPOT 184 W/C, Dow Corning Toray) slabs, so as to producing channels of 3 mm width and 0.1 mm or 1 mm height.

All electrochemical measurements were performed in 50 mM phosphate buffer solution (pH 7.0) containing 0.1 M NaCl at room temperature. The electrochemical properties of the electrodes were characterized using a bipotentiostat (Electrochemical Analyzer, Model 600S, BAS) with three electrode system containing an enzyme-modified electrode as the working electrode, an Ag|AgCl (0.1 M NaCl) reference electrode and a platinum counter electrode. The fuel cell performance was evaluated by measuring the cell voltage while varying the external

resistance between 5 and 200 kΩ. When we evaluated the electrode performance in the various O_2 concentration solutions, we bubbled the reservoir solution with N_2 or O_2. A micro syringe pump (Kd Scientific, Model 210) was used to make a steady flow in the microfluidic channel. The Reynolds number of the flow was small enough to maintain laminar flow.

2.4. Numerical simulations

To asses the shape of the depletion zone of the O_2 in the fluidic channel, we simulated a microfluidic biofuel cell using finite element method software COMSOL multiphysics 3.1 (COMSOL AB) (Fig. 1A″). The simulation was carried out by coupling the Navier–Stokes equation, continuity equation and the mass balance equation, assuming the flow velocity at the surface of the wall is zero (non-slip flow) and O_2 concentration at the surface of the cathode is zero. The diffusion coefficient of O_2 was set to $2 \times 10^{-9} \, m^2 \, s^{-1}$ [27], the bulk concentration of O_2 to $0.2 \, mol \, m^{-3}$, the fluid density to $1 \times 10^3 \, kg \, m^{-3}$, fluid viscosity to $1 \times 10^{-3} \, kg \, m^{-1} \, s^{-1}$ and the average flow velocity to $1.7 \times 10^{-3} \, m \, s^{-1}$. Channel height and cathode length were set to 1 mm and to 10 mm, respectively.

3. Result and discussion

3.1. Linear sweep voltammetry of anode and cathode in a microfluidic channel

Fig. 2a shows linear sweep voltammograms (LSVs) of glucose anode ($2.8 \, mm^2$) in $0.3 \, mL \, min^{-1}$ ($10 \, cm \, min^{-1}$) flow of N_2-bubbled phosphate buffer solution containing 10 mM glucose and 1.0 mM NAD^+ ($\cdots$), with a sigmoidal shape reaching 27 μA (ca. $1 \, mA \, cm^{-2}$). The glucose oxidation current depends
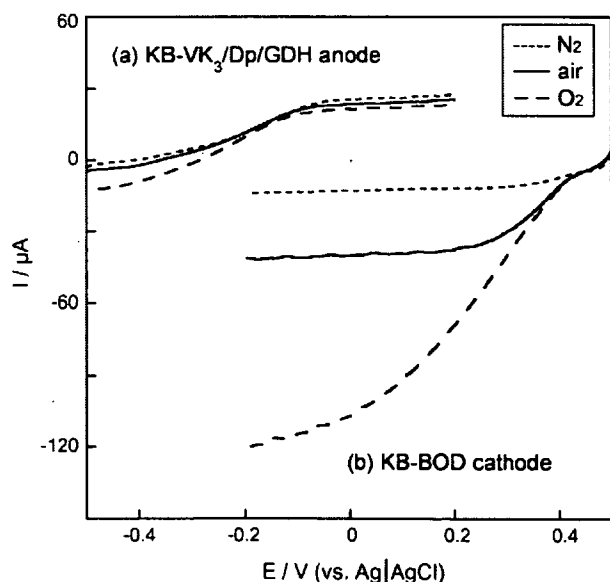

Fig. 2. LSVs of (a) anode and (b) cathode in N_2-bubbled ($\cdots$), air-saturated (—), and O_2-bubbled (---) 50 mM phosphate buffer (pH 7) containing 0.1 M NaCl, 1 mM NAD^+ and 10 mM glucose at room temperature, with a flow rate of $0.3 \, mL \, min^{-1}$. Scan rate: $2 \, mV \, s^{-1}$. Channel height: 1 mm.

on the flow rate as previously reported [6]. The higher flow rate leads to higher current. The glucose oxidation currents obtained in air-saturated solution (—) and O_2-saturated solution (---) were somewhat smaller than that in N_2-bubbled solution, probably because the dissolved O_2 competes with electron relay at the PLL-VK_3/Dp/GDH/KB electrode. In addition to this short-term adverse effect of dissolved O_2 to anode, the irreversible oxidative degradation would occur during longer operation.

The LSVs of BOD-adsorbed KB electrode (10 mm long, $28 \, mm^2$) are shown in Fig. 2b. In N_2-bubbled solution ($\cdots$), only a small current was observed, but in air-saturated (—) and O_2-bubbled solution (---), the O_2 reduction catalytic current clearly appeared at a potential more negative than 0.45 V. The starting potential of O_2 reduction current was about 0.2 V more positive than for the case with Pt electrode as the cathode [6]. This superior performance of a BOD-modified electrode has been already reported by Tsujimura and Kano [8,27–30]. This was due to the direct electron transfer of BOD. The catalytic current reached 41 μA in air saturated solution and 120 μA in O_2-bubbled solution. The shape of LSV was not influenced by the additional presence of NAD^+ and glucose owing to the satisfying reaction selectivity of KB/BOD electrode to O_2 reduction. We have set the flow rate at $10 \, cm \, min^{-1}$, where the diffusion layer of O_2 grows up to a few hundred μm but does not cover the 1 mm channel height, as theoretically discussed later.

As described above, we measured the polarization curve of the glucose electrode and O_2 electrode individually under operating conditions of the fuel cell by using the microfluidic biofuel cell system that internally contains a reference electrode and a counter electrode. In order to balance the current at anode and cathode, we set the area of the cathode ($28 \, mm^2$) ten times larger that the anode ($2.8 \, mm^2$). The combination of these electrodes is expected to show OCV of ca. 0.8 V and maximum current of ca. 25 μA (as limited by anode) in the air-saturated glucose solution. This expected cell performance could be obtained only if the anode is protected from O_2 without decreasing O_2 flux to the cathode.

3.2. O_2 reduction at upstream cathode

With the aim of decreasing the O_2 flux to the anode as simulated in Fig. 1A″, we experimentally studied the effect of pre-reduction of O_2 at a cathode set upstream of the fluidic channel. Fig. 3a shows the currents at the downstream glucose anode versus the O_2 reduction current at the upstream cathode. The glucose oxidation current (at 0 V vs. Ag|AgCl) was successfully increased by the pre-reduction of O_2 by up to 23 μA, nearly equal to that observed in the N_2-bubbled solution (---), suggesting that the degree of decrease in O_2 flux in the vicinity of the anode was sufficient to prevent the adverse reaction of O_2. The pre-reduction should become more significant at lower glucose concentration or higher O_2 concentration due to the relatively larger flux of competitive O_2. The O_2 flux downstream was estimated by experiments using the KB/BOD electrode for both upstream and even downstream (Fig. 3b). The O_2 reduction current (at -0.4 V vs. Ag|AgCl) at the downstream KB/BOD electrode ($I_{O_2 \, at \, downstream}$) decreased linearly with increasing